Materials Horizons

ROYAL SOCIETY OF CHEMISTRY

COMMUNICATION

View Article Online
View Journal | View Issue

Cite this: *Mater. Horiz.*, 2026, **13**, 4147

Received 23rd November 2025,
Accepted 13th February 2026

DOI: 10.1039/d5mh02227d

rsc.li/materials-horizons

Strong hybridization driving unusual enhanced negative thermal expansion in $PbTiO_3$-based ferroelectrics

Zhao Pan, *[ab] Sergey A. Nikolaev, [b] Xi Shen,[a] Takumi Nishikubo,[bc] Lin Wu,[d] Mengqi Ye,[a] Xubin Ye,[a] Shogo Kawaguchi, [f] Yoshihiro Kuroiwa,[d] Richeng Yu, [a] Jun Chen, *[e] Masaki Azuma *[bc] and Youwen Long *[a]

Materials with strong negative thermal expansion (NTE) are crucial for both fundamental research and thermal expansion control engineering. Our previous studies have shown that significantly enhanced NTE can be achieved in $PbTiO_3$–$BiFeO_3$ and $PbTiO_3$–$BiCoO_3$ ferroelectrics by improving the tetragonal distortion (c/a) of the parent $PbTiO_3$. However, the detailed microscopic mechanisms behind this intriguing phenomenon remain unclear. In this study, we explored the temperature-dependent chemical bonding characteristics using high-energy synchrotron X-ray powder diffraction combined with Rietveld refinement, the maximum entropy method, and first-principles calculations. The temperature evolution of the electron density distribution in the ferroelectric phase of $0.5PbTiO_3$–$0.5BiFeO_3$ and $0.6PbTiO_3$–$0.4BiCoO_3$ provides direct evidence of strong covalency, not only in the A-site Pb/Bi–O2 bonds but also in the B-site Ti/Fe/Co–O1 bonds. This covalent character promotes spontaneous polarization through displacements of the highly polarizable A- and B-site cations. Our results reveal that the distinct covalent nature of the Fe–O and Co–O bonds results in contrasting temperature-dependent unit cell volume behaviors, with $PbTiO_3$–$BiFeO_3$ exhibiting strong nonlinear NTE and $PbTiO_3$–$BiCoO_3$ displaying colossal volume contraction. These findings elucidate the microscopic origin of the NTE in $PbTiO_3$-based ferroelectrics and pave the way for the design of new materials with enhanced NTE properties.

New concepts

The discovery of unusual negative thermal expansion (NTE) is of fundamental significance, as it enables the controllable regulation of thermal expansion properties. As a key member of functional materials, $PbTiO_3$-based perovskite ferroelectrics exhibit NTE over a broad temperature range below the Curie temperature (T_C). Notably, favorable enhancement of NTE can be achieved by tailoring the tetragonality of $PbTiO_3$ through chemical substitutions. However, the microscopic mechanisms underlying this intriguing phenomenon remain elusive. This work reported two $PbTiO_3$-based compounds, $0.5PbTiO_3$–$0.5BiFeO_3$ and $0.6PbTiO_3$–$0.4BiCoO_3$, that possess comparable tetragonality yet contrasting NTE behaviors. Our results reveal that the distinct covalent characteristics of Fe–O and Co–O bonds give rise to divergent temperature-dependent unit cell volume responses: $0.5PbTiO_3$–$0.5BiFeO_3$ exhibits strong nonlinear NTE, while $0.6PbTiO_3$–$0.4BiCoO_3$ displays colossal volume contraction. These findings clarify the microscopic origin of NTE in $PbTiO_3$-based ferroelectrics and lay the foundation for the design of advanced materials with enhanced NTE performance.

1. Introduction

Negative thermal expansion (NTE), characterized by material contraction rather than expansion upon heating within a certain temperature range, has attracted considerable interests over the past two decades.[1–5] This intriguing phenomenon has been observed across a diverse range of solids, including alloys, oxides, cyanides, and fluorides, offering opportunities for tailoring the coefficient of thermal expansion (CTE) in single-phase materials or composites.[4–10] A deeper understanding of the mechanisms driving the NTE effect in various classes of solids remains critical. The origin of NTE in widely studied framework materials, such as ZrW_2O_8, $Ag_3[Co(CN_6)]$, and ScF_3, has been attributed to low-frequency phonon vibrations.[11–17] Additionally, several materials exhibit NTE coupled with other

[a] *Beijing National Laboratory for Condensed Matter Physics, Institute of Physics, Chinese Academy of Sciences, Beijing 100190, China. E-mail: zhaopan@iphy.ac.cn, ywlong@iphy.ac.cn*
[b] *Institute of Integrated Research, Institute of Science Tokyo, 4259 Nagatsuta, Midori, Yokohama, 226-8503, Japan. E-mail: mazuma@msl.titech.ac.jp*
[c] *Kanagawa Institute of Industrial Science and Technology (KISTEC), 705-1 Shimoimaizumi, Ebina, Kanagawa, 243-0435, Japan*
[d] *Department of Physical Science, Hiroshima University, Higashihiroshima, Hiroshima, 739-8526, Japan*
[e] *Beijing Advanced Innovation Center for Materials Genome Engineering and Department of Physical Chemistry, University of Science and Technology Beijing, Beijing 100083, China. E-mail: junchen@ustb.edu.cn*
[f] *Research and Utilization Division, Japan Synchrotron Radiation Research Institute (JASRI), SPring-8, 1-1-1 Kouto, Sayo-cho, Sayo-gun, Hyōgo 679-5198, Japan*

physical properties, such as the magnetic transition in Invar alloys and manganese nitrides,[18–20] intermetallic charge transfer in $LaCu_3Fe_4O_{12}$ and $BiNiO_3$,[21–23] and the ferroelectrovolume effect in $PbTiO_3$-based ferroelectrics.[24–27] Notably, stronger NTE effects could enhance the ability to counteract positive thermal expansion in composites. NTE in these functional materials is especially attractive because their CTE can be tuned by modifying the physical properties associated with NTE. Understanding the underlying mechanisms driving NTE presents a unique opportunity to achieve desirable NTE effects and optimize thermal expansion for specific applications.

$PbTiO_3$ (PT) is a prototypical perovskite-type (ABO_3) ferroelectric characterized by high tetragonality (c/a = 1.064) and substantial spontaneous polarization (P_S = 59 μC cm^{-2}) along the polar c-axis.[28] Beyond its renowned ferroelectric properties, PT exhibits unique NTE over the temperature range from room temperature (RT) to its Curie temperature (T_C), with an average volumetric CTE of -1.99×10^{-5} °C^{-1} (RT-490 °C).[29] Due to its structural flexibility, the CTE of PT can be adjusted within a broad range (-0.11 to -5.24×10^{-5} °C^{-1}) through chemical modifications, encompassing the CTE range of other NTE materials.[4] NTE in PT-based ferroelectrics is strongly related to ferroelectricity and is attributed to the spontaneous volume ferroelectrostriction (SVFS) effect.[4,24] As the volume contraction occurs along the polar c-axis, the c/a ratio serves as a useful indicator of NTE.[4,30] A nearly linear correlation between the CTE and the c/a ratio has been observed in PT-based compounds (Fig. 1). Especially, certain PT-based compounds exhibit significantly enhanced NTE through increased tetragonality.[31] For example, $Pb_{0.97}Cd_{0.03}TiO_3$ (-2.16×10^{-5} °C^{-1}, c/a = 1.067), $0.8PbTiO_3$–$0.2BiCoO_3$ (-3.78×10^{-5} °C^{-1}, c/a = 1.089), and $0.5PbTiO_3$–$0.5BiFeO_3$ (-4.15×10^{-5} °C^{-1}, c/a = 1.141) exhibit enhanced NTE.[32,33] In addition, the strong NTE of tetragonal $0.5PbTiO_3$–$0.5BiFeO_3$ can be fine-tuned from negative to near-zero thermal expansion (-0.71×10^{-5} °C^{-1}, $0.5PbTiO_3$–$0.5Bi_{0.8}La_{0.2}FeO_3$, c/a = 1.057) by reducing tetragonality through the substitution of Bi^{3+} with La^{3+}.[24] However, the relationship between the CTE and the c/a ratio is less consistent in materials with enhanced NTE compared to those with weakened NTE (Fig. 1). Furthermore, distinct NTE behaviors have been observed in compounds with similar tetragonalities, such as the nonlinear strong NTE from RT to T_C and significant volume contraction during the ferroelectric-to-paraelectric phase transition in $0.5PbTiO_3$–$0.5BiFeO_3$ and $0.6PbTiO_3$–$0.4BiCoO_3$, respectively.[24,33] A critical unresolved issue is understanding the correlation between NTE and ferroelectricity in PT-based ferroelectrics. Ferroelectricity in perovskite-type ferroelectrics is known to arise from hybridization between the A/B-site cations and oxygen.[34,35] The distinct NTE behaviors in $0.5PbTiO_3$–$0.5BiFeO_3$ (0.5PT–0.5BF) and $0.6PbTiO_3$–$0.4BiCoO_3$ (0.6PT–0.4BC) are likely related to differences in their ferroelectric activities. While it has been suggested that the temperature-dependent evolution of the electronic structure could elucidate the origin of NTE in PT-based ferroelectrics, few studies have explored the relationship between A/B–O hybridization and thermal expansion behavior.

In this study, high-energy synchrotron X-ray powder diffraction (SXRD) was performed on two representative compounds: 0.5PT–0.5BF and 0.6PT–0.4BC, which show similar tetragonalities while demonstrating two different types of nonlinear strong NTE and significant volume contraction, respectively. The electron density distribution was analyzed using experimental Rietveld refinement and the maximum entropy method (MEM), combined with first-principles electronic structure calculations. Our analysis provides direct experimental evidence of strong Pb/Bi–O2 and Ti/Fe/Co–O1 hybridizations, revealed by covalent bonding electron distribution. These results suggest that the strong covalency in cation-oxygen bonds is closely correlated with unusual physical properties, including large lattice distortions, high T_C, and enhanced NTE or significant volume contraction.

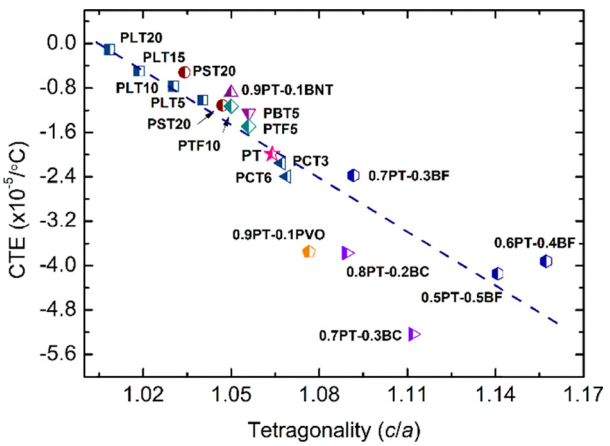

Fig. 1 Average volumetric CTE as a function of the c/a ratio in $PbTiO_3$-based ferroelectrics.[4,25,33] Among those materials, PLT100x is the abbreviation of $Pb_{1-x}La_xTiO_3$, PST100x represents $Pb_{1-x}Sr_xTiO_3$, PTF100x stands for $Pb(Ti_{1-x}Fe_x)O_3$, PBT100x represents $(Pb_{1-x}Bi_x)TiO_3$, (1 − x)PT–xBNT represents (1 − x)$PbTiO_3$–$xBi(Ni_{1/2}Ti_{1/2})O_3$, PCT100x stands for $Pb_{1-x}Cd_xTiO_3$, (1 − x)PT–xPV represents (1 − x)$PbTiO_3$–$xPbVO_3$, (1 − x)PT–xBF represents (1 − x)$PbTiO_3$–$xBiFeO_3$, and (1 − x)PT–xBC represents (1 − x)$PbTiO_3$–$xBiCoO_3$.

2. Results and discussion

The 0.5PT–0.5BF sample was prepared using a traditional solid-state method, whereas the 0.6PT–0.4BC compound was synthesized using high-pressure and high-temperature methods. High-temperature SXRD data were collected at the BL02B2 beamline at SPring-8. To ensure precise electron density mapping, accurate Bragg-integrated intensity data were collected. High-energy SXRD data were obtained to analyze both the tetragonal and cubic phases of 0.5PT–0.5BF and 0.6PT–0.4BC. High-energy SXRD proved particularly effective in minimizing absorption effects caused by the heavy elements Pb and Bi. Details regarding structural parameters and additional related information are provided in the SI.

Rietveld refinements of the SXRD data for 0.5PT–0.5BF (Fig. 2a) and 0.6PT–0.4BC (Fig. 2b) at 300 K were successfully

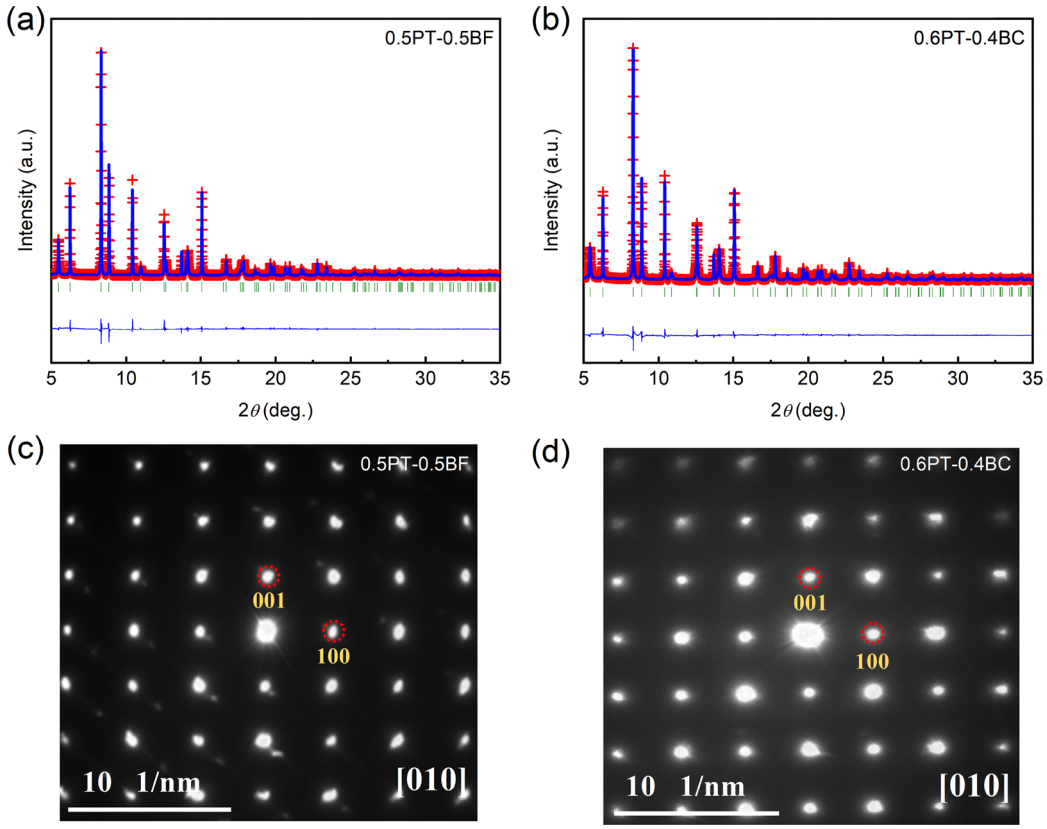

Fig. 2 Rietveld refinement for the (a) 0.5PT–0.5BF and (b) 0.6PT–0.4BC compounds at room temperature. The SAED patterns of the (c) 0.5PT–0.5BF and (d) 0.6PT–0.4BC compounds along the [010] zone axis. The red circles show the spots that can be indexed with a prototype tetragonal structure with the space group *P*4*mm*.

performed based on a tetragonal perovskite structure with the space group *P*4*mm*. Both compounds exhibited similar tetragonalities, with c/a = 1.141 and c/a = 1.143, respectively, which are significantly higher than that of undoped PT.[31] The SAED patterns of the 0.5PT–0.5BF and 0.6PT–0.4BC compounds along the [010] zone axis at room temperature have further confirmed their tetragonal structure (Fig. 2c and d). Based on SAED analysis, we can obtain the lattice parameters of $a(b)$ = 3.8582 Å, c = 4.4011 Å and $a(b)$ = 3.8411 Å, c = 4.3946 Å, yielding c/a ratios of 1.141 and 1.144 for the 0.5PT–0.5BF and 0.6PT–0.4BC compounds, respectively. The results are in good agreement with the Rietveld refinements of the SXRD data. In PT-based compounds, an increase in the c/a ratio is usually associated with enhanced NTE.[4] However, the temperature dependence of the unit cell volume reveals two different types of NTE behavior in 0.5PT–0.5BF and 0.6PT–0.4BC. As illustrated in Fig. 3, 0.5PT–0.5BF exhibits nonlinear, enhanced NTE over a broad temperature range from RT to 640 °C, with a coefficient of -4.13×10^{-5} °C^{-1} (Fig. 3c). Conversely, 0.6PT–0.4BC undergoes a sudden volume shrinkage as large as −3.2% during the ferroelectric-to-paraelectric phase transition(Fig. 3d), while the unit cell volume demonstrates minimal temperature dependence below T_C. Interestingly, strong nonlinear NTE was also observed in 0.7PT–0.3BC, which has a smaller tetragonality (c/a = 1.112), and a larger volume contraction of 4.8% was found in 0.5PT–0.5BC, which has a higher tetragonality (c/a = 1.169) (Fig. S1). These contrasting NTE behaviors are believed to correlate with differences in ferroelectric properties. Recently, a new concept, SVFS (ω_S), was proposed to quantitatively describe the effect of ferroelectricity on NTE.[24] The SVFS is defined as follows:

$$\omega_S = \frac{V_{exp} - V_{nm}}{V_{nm}} \times 100\%,$$

where V_{exp} and V_{nm} are unit cell volumes of the experimental and nominal structures, respectively. V_{nm} is estimated by extrapolating between the paraelectric and ferroelectric phases. The ω_S values for 0.5PT–0.5BF and 0.6PT–0.4BC were determined to be 5.3% and 8.0%, respectively (Fig. 3c and d), substantially higher than that of parent PT (3.1%). A higher ω_S value indicates stronger NTE, suggesting that the SVFS effect provides a qualitative explanation for the enhanced NTE in PT-based ferroelectrics. However, despite similar tetragonalities, the underlying reasons for the different NTE behaviors observed in these materials remain unclear, highlighting the need for further investigation.

Since the unit cell volume in PT-based ferroelectrics is mainly controlled by the evolution of the *c*-axis,[4,30] the c/a ratio serves as an effective parameter for tracing NTE. As illustrated in Fig. 3a and b, the temperature dependence of the lattice

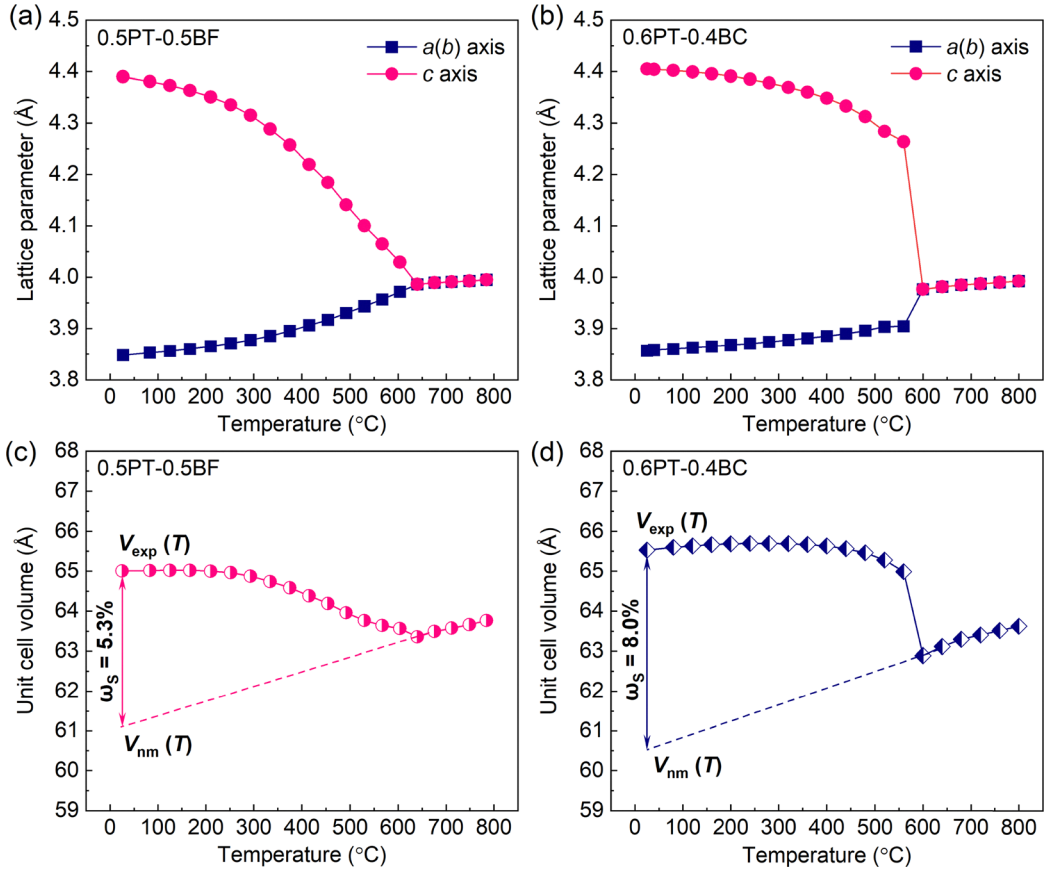

Fig. 3 Lattice parameters of $a(b)$ and c for the (a) 0.5PT–0.5BF and (b) 0.6PT–0.4BC compounds, and the corresponding unit cell volume as a function of temperature for the (c) 0.5PT–0.5BF and (d) 0.6PT–0.4BC compounds. An illustration of ω_S is also provided.

parameters for 0.5PT–0.5BF and 0.6PT–0.4BC reveals that the a and b-axes show similar steady increases in both systems. However, the c-axis demonstrates strong temperature dependence, demonstrating a marked contrast between the two compounds. In 0.5PT–0.5BF, the c-axis decreases continuously and almost linearly with increasing temperature, consistent with the observed enhanced NTE. Conversely, in 0.6PT–0.4BC, the c-axis decreases more slowly at temperatures below T_C and exhibits steady temperature dependence in the ferroelectric phase until a dramatic shrinkage occurs as the temperature approaches T_C. This behavior corresponds to the distinct evolution of the c/a ratio as a function of temperature for 0.5PT–0.5BF and 0.6PT–0.4BC (Fig. S2a), in which 0.6PT–0.4BC shows a more stable c/a ratio than 0.5PT–0.5BF in the ferroelectric phase. Correspondingly, a pronounced volume contraction was observed in 0.6PT–0.4BC during the ferroelectric-to-paraelectric phase transition. These results confirm that the NTE behavior in PT-based compounds is predominantly governed by the c-axis. The large lattice distortions responsible for these behaviors are attributed to strong spontaneous polarization (P_S). In perovskite-type ferroelectrics, P_S originates from the displacement of the centroids of the oxygen polyhedra surrounding the A- and B-site atoms. The SXRD refinement results were used to derive the P_S displacements of the A-site (δz_A) and B-site (δz_B) cations, as illustrated in Fig. S2b. For 0.6PT–0.4BC, both δz_A and δz_B are larger than those of 0.5PT–0.5BF, indicating stronger ferroelectricity in 0.6PT–0.4BC. Furthermore, different temperature-dependent behaviors are observed for these displacements. In 0.5PT–0.5BF, δz_A and δz_B decrease continuously with increasing temperature, exhibiting nonlinear behavior. In contrast, δz_A and δz_B in 0.6PT–0.4BC remain stable with a linear trend in the ferroelectric phase. However, as T_C is approached, a sharp decrease in δz_B is observed in 0.6PT–0.4BC.

Neglecting electronic polarization and considering a simple ionic crystal, P_S can be estimated using the following expression:[36]

$$P_S = Z\sum_i \frac{\delta z_i q_i}{V},$$

where δz_i represents the cation shift along the ferroelectric axis for the ith ion with electric charge q_i, V is the unit cell volume, and $Z = 1$. The calculated P_S values for 0.5PT–0.5BF and 0.6PT–0.4BC as functions of temperature are shown in Fig. S2c. Similar to the trends observed for c/a and δz, P_S decreases continuously with temperature in 0.5PT–0.5BF but decreases more gradually in 0.6PT–0.4BC. These results further confirm that ferroelectricity plays a crucial role in the NTE of PT-based ferroelectrics.

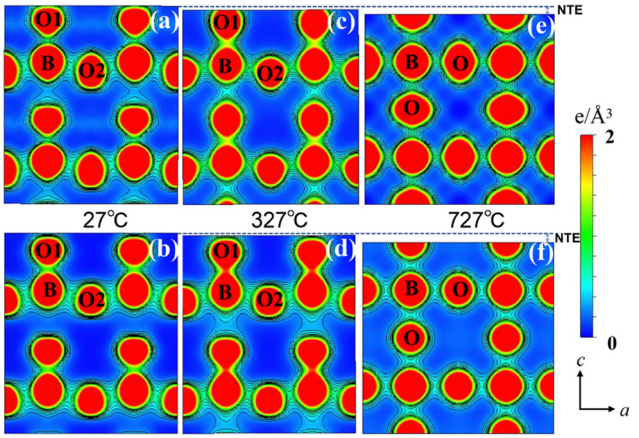

Fig. 4 Electron density distribution on the (020) planes of tetragonal ferroelectric 0.5PT–0.5BF at (a) 27 °C and (c) 400 °C, and 0.6PT–0.4BC at (b) 27 °C and (d) 400 °C, as well as cubic paraelectric 0.5PT–0.5BF at (e) 800 °C and 0.6PT–0.4BC at (f) 800 °C from synchrotron diffraction data. Contours are shown from 0.3 to 1 $Å^{-3}$ by 0.1 $Å^{-3}$ step in (a)–(f). The dashed line indicates the role of spontaneous polarization (δ_B) in NTE.

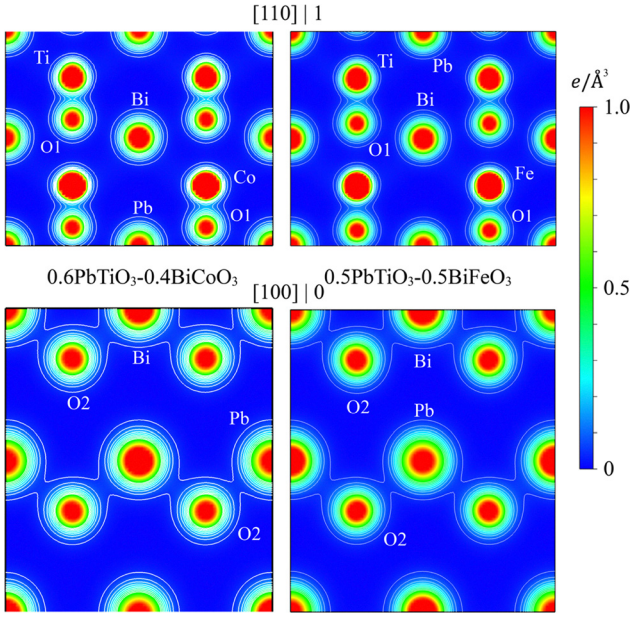

Fig. 5 Charge density distribution of $0.6PbTiO_3$–$0.4BiCoO_3$ (left) and $0.5PbTiO_3$–$0.5BiFeO_3$ (right) as obtained from electronic structure calculations. The results are shown for the planes [110]|1 (top) and [100]|0 (bottom). Contours are plotted with an interval of 0.05 e $Å^{-3}$. The results are obtained for experimental crystal structures at 27 °C.

It is well established that hybridization between A/B-site cations and oxygen is essential for ferroelectricity in PT-based compounds.[34,35] However, limited information exists regarding chemical bonding in NTE ferroelectrics.[35,37] The different NTE behaviors observed in 0.5PT–0.5BF and 0.6PT–0.4BC can be attributed to differences in the covalency of the A/B-site cation-oxygen bonds. To explore this further, we investigated the temperature dependence of the electron density distribution within the NTE temperature range for both compounds. Rietveld refinements of the SXRD patterns for the tetragonal ferroelectric phase (27 °C and 400 °C) and cubic paraelectric phase (800 °C) of 0.5PT–0.5BF and 0.6PT–0.4BC were successfully performed based on the tetragonal *P4mm* and cubic $Pm\bar{3}m$ space groups, respectively (Fig. S3 and Tables S1, S2). The two-dimensional (2D) electron density distributions obtained *via* MEM/Rietveld analysis are illustrated in Fig. 4. In the cubic phase at 800 °C, the MEM electron density distributions for the six (Fe, Ti)/(Co, Ti)–O bonds are isotropic and predominantly ionic. Conversely, in the tetragonal phase, the electron density around the (Fe, Ti)/(Co, Ti) atoms becomes highly anisotropic, attributed to the presence of shorter and longer B–O bonds. The shorter (Fe, Ti)–O1 and (Co, Ti)–O1 bonds in the tetragonal 0.5PT–0.5BF (Fig. 4a and c) and 0.6PT–0.4BC (Fig. 5b and d) at 27 °C and 400 °C are covalent, while (Fe, Ti)–O and (Co, Ti)–O bonds in the cubic 0.5PT–0.5BF and 0.6PT–0.4BC at 800 °C are more ionic (Fig. 4e and f). This covalent nature is supported by the hybridization of (Fe, Ti)/(Co, Ti) 3d and O 2p orbitals, as illustrated in the density of states (Fig. S4 and S5). Notably, the (Co, Ti)–O1 bond in 0.6PT–0.4BC exhibits stronger covalency (minimum electron density (MED) = 1.13 $Å^{-3}$ at 27 °C and MED = 1.90 $Å^{-3}$ at 400 °C) compared to the (Fe, Ti)–O1 bond in 0.5PT–0.5BF (MED = 0.84 $Å^{-3}$ at 27 °C and MED = 1.41 $Å^{-3}$ at 400 °C). This is further evidenced by the shorter bond lengths of (Co, Ti)–O1(1.72 Å at 27 °C and 1.71 Å at 400 °C) compared to (Fe, Ti)–O1 (1.83 Å at 27 °C and 1.83 Å at 400 °C). The stronger covalency in 0.6PT–0.4BC suggests a more significant hybridization effect of (Co, Ti)–O1, which is crucial for the SVFS effect.[4,24] As a result, ferroelectricity in 0.6PT–0.4BC is better maintained in the ferroelectric phase compared to 0.5PT–0.5BF. In the cubic paraelectric phase, the covalent bonds in both compounds transform into ionic bonds, resulting in the disappearance of ferroelectricity. This transformation explains the different NTE behaviors observed in 0.5PT–0.5BF and 0.6PT–0.4BC.

The covalent character of the A–O bonds in 0.5PT–0.5BF and 0.6PT–0.4BC was also investigated. The 2D electron density distributions for these compounds at 27, 400, and 800 °C are displayed in Fig. S6. The shorter (Pb, Bi)–O2 bonds in the tetragonal phases of both 0.5PT–0.5BF and 0.6PT–0.4BC exhibit strong covalency in the ferroelectric phase, transitioning to the predominantly ionic character in the high-temperature cubic phase. Notably, the covalent (Pb, Bi)–O2 bond in 0.6PT–0.4BC (MED = 0.57 $Å^{-3}$ at 27 °C and MED = 0.55 $Å^{-3}$ at 400 °C) is slightly stronger than that in 0.5PT–0.5BF (MED = 0.48 $Å^{-3}$ at 27 °C and MED = 0.46 $Å^{-3}$ at 400 °C). This stronger hybridization between Pb/Bi and O in 0.6PT–0.4BC contributes to its more pronounced SVFS effect compared to 0.5PT–0.5BF.

To gain further insight into the hybridization of $0.6PbTiO_3$–$0.4BiCoO_3$ and $0.5PbTiO_3$–$0.5BiFeO_3$ from a microscopic perspective, we carry out electronic structure calculations (Fig. 5). The detailed information is provided in SI. As covalency in B–O bonds is related to the degree of orbital mixing between the transition-metal 3d and O 2p states, fundamental features can be understood qualitatively by considering differences in electronegativity, orbital occupancy, and the energy mismatch

between the 3d and O 2p states. In $PbTiO_3$, Ti^{4+} has a $3d^0$ electronic configuration. In contrast, Co^{3+} in $BiCoO_3$ and Fe^{3+} in $BiFeO_3$ adopt high-spin $3d^6$ and $3d^5$ electronic configurations, respectively. Co^{3+} is more electronegative than Fe^{3+},[38] as its higher ionic charge and smaller radius outweigh the shielding from its extra *d* electron. Consequently, a stronger pull on the cloud of bonding electrons is expected in the case of Co^{3+} relative to Fe^{3+}, resulting in a more covalent character and shorter Co–O bond lengths. The greater covalent character of Co–O bonds gives rise to stronger ferroelectricity in 0.6PT–0.4BC, thereby enhancing the SVFS effect and leading to the large NTE observed in 0.6PT–0.4BC.

NTE materials are highly desirable for thermal expansion control engineering. Particularly, materials with strong NTE can serve as high-performance thermal expansion compensators. $PbTiO_3$ is a typical perovskite ferroelectric which also exhibits unique NTE behavior. The flexible structure of $PbTiO_3$ allows for the achievement of large NTE by modulating its tetragonality through the incorporation of suitable cations in A/B sites,[4] or even at the anion oxygen site.[4,39] While the spontaneous volume ferroelectrostriction effect has been proposed to account for the unusual thermal expansion behavior in $PbTiO_3$-based ferroelectric NTE materials, the microscopic mechanisms underlying this intriguing phenomenon still remain to be fully explored. Herein, for the first time, we investigated the temperature-dependent chemical bonding characteristics using high-energy SXRD combined with Rietveld refinement and the maximum entropy method, supported by first-principles calculations, revealing the mechanism of NTE in $PbTiO_3$-based ferroelectrics from a microscopic perspective. It is worth noting that beyond the above-mentioned bond covalency, other possible contributions – such as differences in ionic size, electronegativities, and bond stiffness – may potentially affect the crystal and electronic structure, thereby modifying the NTE behavior of $PbTiO_3$-based ferroelectrics. While these factors are expected to influence the NTE behavior, their specific roles remain to be fully verified. Consequently, further studies are necessary to clarify these intrinsic mechanisms in the future.

3. Conclusion

In summary, we address an important issue of chemical bonding in $PbTiO_3$-based ferroelectrics with enhanced NTE. By combining MEM analysis of synchrotron diffraction data with first-principles calculations for 0.5PT–0.5BF and 0.6PT–0.4BC, we accurately determined the temperature-dependent electron density distributions. Our results provide direct evidence of strong hybridization between the (Pb, Bi)(6s, 6p)/(Fe, Co/Ti)(3d) and O(2p) orbitals, which play a crucial role in the large tetragonalities and unusually enhanced NTE observed in both systems. Despite their similar tetragonalities, the differing covalencies in the (Co, Ti)–O and (Fe, Ti)–O bonds are mainly responsible for the different NTE behaviors. These differences result in significant volume contraction in 0.6PT–0.4BC and nonlinearly enhanced thermal expansion in 0.5PT–0.5BF. These findings contribute to a deeper understanding of the physical and chemical properties of $PbTiO_3$-based ferroelectrics and pave the way for the design of novel materials with enhanced NTE properties.

4. Experimental section

Sample preparation

The $0.5PbTiO_3$–$0.5BiFeO_3$ (0.5PT–0.5BF) compound was synthesized by the conventional solid-sate method. The raw materials PbO, Bi_2O_3, TiO_2, and Fe_2O_3 are mixed according to the stoichiometric ratio, and calcined in a covered crucible at 800 °C for 5 h. Part of the calcined powders were pressed into pellets and then sintered at 1150 °C for 2 h covered with the remaining powders to compensate the volatilization of PbO and Bi_2O_3 during the sintering process. The surface layers of sintered pellets were removed, carefully crushed, and then annealed at 600 °C for 1 h to remove the mechanical strain introduced during the sintering and grinding processes. The $0.6PbTiO_3$–$0.4BiCoO_3$ (0.6PT–0.4BC) compound was prepared with a cubic anvil-type high-pressure apparatus. Stoichiometric mixture powder of PbO, TiO_2, Bi_2O_3, and Co_3O_4 was sealed in a gold capsule and reacted at 6 GPa and 1373 K for 30 min. 10 mg amount of the oxidizing agent $KClO_4$ (about 10 wt% of the sample) was separately added to the top and bottom of the capsule. The obtained sample was crushed and washed with distilled water to remove the remaining KCl.

Structure analysis

The room-temperature crystal structures of 0.5PT–0.5BF and 0.6PT–0.4BC were extracted from synchrotron X-ray diffraction (SXRD) data collected at beam line BL02B2 of SPring-8 with wavelength λ = 0.42 Å. The temperature dependence of SXRD data of 0.5PT–0.5BF and 0.6PT–0.4BC were also performed at beam line BL02B2 of SPring-8 with the same wavelength of λ = 0.42 Å. The detailed crystal structure was refined based on the full-profile Rietveld method performed on the software FULLPROF. Selected area electron diffraction (SAED) was performed at room temperature using a JEOL ARM200F transmission electron microscope equipped with double Cs correctors (CEOS) for the condenser and objective lens along the [010] zone axis.

Electronic structure calculation

Electronic structure calculations were performed within generalized gradient approximation[40] for the exchange correlation functional using the projected augmented wave method,[41] as implemented in the Vienna *Ab initio* Simulation Package.[42] The plane-wave cut-off energy was set to 500 eV, and the total energy convergence criterion was 10^{-8} eV for all calculations. Electronic correlations in the d shell of the magnetic ions were accounted for using the GGA+*U* method.[43] The effect of spin–orbit coupling was neglected in all calculations on account of its relative smallness.

Author contributions

Z. P. conceived the project. Z. P. synthesized the samples. S. A. N. performed the theoretical calculations, and interpreted the results with Z. P. Z. P., X. B. Y., T. N., and S. K. performed the synchrotron X-ray diffraction experiments. L. W. performed the maximum entropy method calculation, with assistance from Y. K. X. S. and R. Y. measured and analyzed the TEM data. Z. P. wrote the manuscript. All authors discussed the results and commented on the manuscript. Z. P., J. C. M. A., and Y. L. guided the projects.

Conflicts of interest

The authors declare that they have no competing interests.

Data availability

The data that support the findings of this study are available in the supplementary information (SI) of this article. The supplementary information includes part of the detailed electronic structure calculation methods, additional characterization data, and supporting figures and tables related to this study. See DOI: https://doi.org/10.1039/d5mh02227d.

Acknowledgements

This work was partially supported by the National Natural Science Foundation of China (Grant No. 22271309, 12425403, 12304268, and 12261131499), the National Key R&D Program of China (Grant No. 2021YFA1400300 and 2025YFE0202100), the Grants-in-Aids for Scientific Research JP18H05208, JP19H05625, JP24K17509, and JP24H00374 from the Japan Society for the Promotion of Science (JSPS), the Beijing Natural Science Foundation (No. F251005), JSTCREST (JPMJCR22O1), and the Kanagawa Institute of Industrial Science and Technology. The synchrotron radiation experiments were performed at SPring-8 with the approval of the Japan Synchrotron Radiation Research Institute (2019A1045, 2023B1575, and 2025A1495).

References

1 T. A. Mary, J. S. O. Evans, T. Vogt and A. W. Sleight, *Science*, 1996, **272**, 90.
2 J. S. O. Evans, *J. Chem. Soc., Dalton Trans.*, 1999, **19**, 3317.
3 K. Takenaka, *Sci. Technol. Adv. Mater.*, 2012, **13**, 013001.
4 J. Chen, L. Hu, J. X. Deng and X. R. Xing, *Chem. Soc. Rev.*, 2015, **44**, 3522.
5 Z. Pan, T. Nishikubo, H. Yamamoto, X. B. Ye, M. Azuma and Y. W. Long, *cMat*, 2025, **2**, e70017.
6 J. M. Gou, Y. Pan, X. L. Liu, C. Liu, H. L. Zhang, D. Liu, X. G. Xu, C. X. Liang, X. F. Zhang and T. Y. Ma, *Adv. Mater.*, 2025, **37**, e07767.
7 Y. Song, J. Chen, X. Liu, C. Wang, J. Zhang, H. Liu, H. Zhu, L. Hu, K. Lin, S. Zhang and X. Xing, *J. Am. Chem. Soc.*, 2018, **140**, 602.
8 N. Shi, A. Sanson, Q. Gao, Q. Sun, Y. Ren, Q. Huang, D. O. de Souza, X. Xing and J. Chen, *J. Am. Chem. Soc.*, 2020, **142**, 3088.
9 Q. Gao, J. Chen, Q. Sun, D. Chang, Q. Huang, H. Wu, A. Sanson, R. Milazzo, H. Zhu, Q. Li, Z. Liu, J. Deng and X. Xing, *Angew. Chem.*, 2017, **129**, 9151.
10 D. Wendt, E. Bozin, J. Neuefeind, K. Page, W. Ku, L. Wang, B. Fultz, A. V. Tkachenko and I. A. Zaliznyak, *Sci. Adv.*, 2019, **5**, eaay2748.
11 R. Mittal and S. L. Chaplot, *Phys. Rev. B: Condens. Matter Mater. Phys.*, 1999, **60**, 7234.
12 R. Mittal, S. L. Chaplot, H. Schober and T. A. Mary, *Phys. Rev. Lett.*, 2001, **86**, 4692.
13 A. L. Goodwin, M. Calleja, M. J. Conterio, M. T. Dove, J. S. O. Evans, D. A. Keen, L. Peters and M. G. Tucker, *Science*, 2008, **319**, 794.
14 B. K. Greve, K. L. Martin, P. L. Lee, P. J. Chupas, K. W. Chapman and A. P. Wilkinson, *J. Am. Chem. Soc.*, 2010, **132**, 15496.
15 C. W. Li, X. Tang, J. A. Muñoz, J. B. Keith, S. J. Tracy, D. L. Abernathy and B. Fultz, *Phys. Rev. Lett.*, 2011, **107**, 195504.
16 L. Hu, J. Chen, L. Fan, Y. Ren, Y. Rong, Z. Pan, J. Deng, R. Yu and X. Xing, *J. Am. Chem. Soc.*, 2014, **136**, 13566.
17 J. Chen, Q. Gao, A. Sanson, X. Jiang, Q. Huang, A. Carnera, C. G. Rodriguez, L. Olivi, L. Wang, L. Hu, K. Lin, Y. Ren, Z. Lin, C. Wang, L. Gu, J. Deng, J. P. Attfield and X. Xing, *Nat. Commun.*, 2017, **8**, 14441.
18 P. Mohn, *Nature*, 1999, **400**, 18.
19 K. Takenaka and H. Takagi, *Appl. Phys. Lett.*, 2005, **87**, 261902.
20 X. L. Yuan, B. Wang, Y. Sun, H. M. Guo, K. W. Shi, S. H. Deng, L. H. He, H. Q. Lu, H. Zhang, S. D. Xu, W. C. Hao, S. Q. Chu, Z. J. Ma, S. H. An, J. Cui, D. M. Hu, H. M. Han and C. Wang, *Adv. Funct. Mater.*, 2024, **34**, 2404629.
21 Y. W. Long, N. Hayashi, T. Saito, M. Azuma, S. Muranaka and Y. Shimakawa, *Nature*, 2009, **458**, 60.
22 M. Azuma, W. T. Chen, H. Seki, M. Czapski, S. Olga, K. Oka, M. Mizumaki, T. Watanuki, N. Ishimatsu, N. Kawamura, S. Ishiwata, M. G. Tucker, Y. Shimakawa and J. P. Attfield, *Nat. Commun.*, 2011, **2**, 347.
23 T. Nishikubo, Y. Sakai, K. Oka, T. Watanuki, A. Machida, M. Mizumaki, K. Maebayashi, T. Imai, T. Ogata, K. Yokoyama, Y. Okimoto, S. Kosshihara, H. Hojo, T. Mizokawa and M. Azuma, *J. Am. Chem. Soc.*, 2019, **141**, 19397.
24 J. Chen, F. F. Wang, Q. Z. Huang, L. Hu, X. P. Song, J. X. Deng, R. B. Yu and X. R. Xing, *Sci. Rep.*, 2013, **3**, 2458.
25 Z. Pan, J. Chen, X. Jiang, L. Hu, R. Yu, H. Yamamoto, T. Ogata, Y. Hattori, F. Guo, X. Fan, Y. Li, G. Li, H. Gu, Y. Ren, Z. Lin, M. Azuma and X. R. Xing, *J. Am. Chem. Soc.*, 2017, **139**, 14865.
26 Z. Pan, F. Y. Zhou, M. Q. Ye, D. Wang, Q. M. Liu, T. Nishikubo, X. B. Ye, X. Wang, J. Liu, N. P. Lu, S. Kawaguchi, M. Azuma and Y. W. Long, *J. Adv. Ceram.*, 2025, **14**, 9221096.

27 Z. Pan, Z. L. Liang, X. Wang, Y.-W. Fang, X. B. Ye, Z. H. Liu, T. Nishikubo, Y. Sakai, X. Shen, Q. M. Liu, S. Kawaguchi, F. Zhan, L. L. Fan, Y.-Y. Wang, C.-Y. Ma, X. X. Jiang, Z. S. Lin, R. C. Yu, X. R. Xing, M. Azuma and Y. W. Long, *Mater. Horiz.*, 2024, **11**, 5394.
28 S. C. Abrahams, S. K. Kurtz and P. B. Jamieson, *Phys. Rev.*, 1968, **172**, 551.
29 J. Chen, X. R. Xing, R. B. Yu and G. R. Liu, *J. Am. Ceram. Soc.*, 2005, **88**, 1356.
30 J. Chen, X. R. Xing, C. Sun, P. H. Hu, R. B. Yu, X. W. Wang and L. H. Li, *J. Am. Chem. Soc.*, 2008, **130**, 1144.
31 G. Shirane, S. Hoshino and K. Suzuki, *J. Phys. Soc. Jpn.*, 1950, **5**, 453.
32 J. Chen, X. R. Xing, G. R. Liu, J. H. Li and Y. T. Liu, *Appl. Phys. Lett.*, 2006, **89**, 101914.
33 Z. Pan, J. Chen, R. Z. Yu, L. Patra, P. Ravindran, A. Sanson, R. Milazzo, A. Carnera, L. Hu, L. Wang, H. Yamamoto, Y. Ren, Q. Z. Huang, Y. Sakai, T. Nishikubo, T. Ogata, X. A. Fan, Y. W. Li, G. Q. Li, H. Hojo, M. Azuma and X. R. Xing, *Chem. Mater.*, 2019, **31**, 1296.
34 R. E. Cohen, *Nature*, 1992, **358**, 136.
35 Y. Kuroiwa, S. Aoyagi, A. Sawada, J. Harada, E. Nishibori, M. Takata and M. Sakata, *Phys. Rev. Lett.*, 2001, **87**, 217601.
36 J. Frantti, S. Ivanov, S. Eriksson, H. Rundlöf, V. Lantto, J. Lappalainen and M. Kakihana, *Phys. Rev. B: Condens. Matter Mater. Phys.*, 2002, **66**, 064108.
37 L. Fan, Q. Li, L. Zhang, N. Shi, H. Liu, Y. Ren, J. Chen and X. Xing, *Inorg. Chem. Front.*, 2020, **7**, 1190.
38 K. Y. Li and D. F. Xue, *J. Phys. Chem. A*, 2006, **110**, 11332.
39 Z. Pan, Y.-W. Fang, S. A. Nikolaev, L. Wu, J. Zhang, M. Q. Ye, J. Liu, X. B. Ye, X. Wang, T. Nishikubo, Y. Sakai, R. Z. Yu, S. Kawaguchi, N. P. Lu, Y. kuroiwa, J. Chen, M. Azuma, X. R. Xing and Y. W. Long, *Mater. Horiz.*, 2025, **12**, 6804.
40 J. P. Perdew, K. Burke and M. Ernzerhof, *Phys. Rev. Lett.*, 1996, **77**, 3865.
41 P. E. Blochl, *Phys. Rev. B: Condens. Matter Mater. Phys.*, 1994, **50**, 17953.
42 G. Kresse and J. Hafner, *Phys. Rev. B: Condens. Matter Mater. Phys.*, 1993, **47**, 558.
43 A. I. Liechtenstein, V. I. Anisimov and J. Zaane, *Phys. Rev. B: Condens. Matter Mater. Phys.*, 1995, **52**, R5467.

